JVI Journals.ASM.org

Mapping a Neutralizing Epitope onto the Capsid of Adeno-Associated Virus Serotype 8

Brittney L. Gurda,[a]* Christina Raupp,[b]* Ruth Popa-Wagner,[b] Matthias Naumer,[b] Norman H. Olson,[c] Robert Ng,[a] Robert McKenna,[a] Timothy S. Baker,[c] Jürgen A. Kleinschmidt,[b] and Mavis Agbandje-McKenna[a]

Department of Biochemistry and Molecular Biology, University of Florida, Gainesville, Florida, USA[a]; German Cancer Research Center, Heidelberg, Germany[b]; and Department of Chemistry and Biochemistry and Division of Biological Sciences, University of California-San Diego, La Jolla, California, USA[c]

Adeno-associated viruses (AAVs) are small single-stranded DNA viruses that can package and deliver nongenomic DNA for therapeutic gene delivery. AAV8, a liver-tropic vector, has shown great promise for the treatment of hemophilia A and B. However, as with other AAV vectors, host anti-capsid immune responses are a deterrent to therapeutic success. To characterize the antigenic structure of this vector, cryo-electron microscopy and image reconstruction (cryo-reconstruction) combined with molecular genetics, biochemistry, and *in vivo* approaches were used to define an antigenic epitope on the AAV8 capsid surface for a neutralizing monoclonal antibody, ADK8. Docking of the crystal structures of AAV8 and a generic Fab into the cryo-reconstruction for the AAV8-ADK8 complex identified a footprint on the prominent protrusions that flank the 3-fold axes of the icosahedrally symmetric capsid. Mutagenesis and cell-binding studies, along with *in vitro* and *in vivo* transduction assays, showed that the major ADK8 epitope is formed by an AAV variable region, VRVIII (amino acids 586 to 591 [AAV8 VP1 numbering]), which lies on the surface of the protrusions facing the 3-fold axis. This region plays a role in AAV2 and AAV8 cellular transduction. Coincidently, cell binding and trafficking assays indicate that ADK8 affects a postentry step required for successful virus trafficking to the nucleus, suggesting a probable mechanism of neutralization. This structure-directed strategy for characterizing the antigenic regions of AAVs can thus generate useful information to help re-engineer vectors that escape host neutralization and are hence more efficacious.

The adeno-associated viruses (AAVs), members of the *Dependovirus* genus of the single-stranded DNA (ssDNA) *Parvoviridae*, are promising gene transfer vectors owing to their ability to transduce both nondividing and dividing cells. These viruses require helper functions from adenovirus or herpes simplex virus to yield a productive infection, but such infection is not associated with any disease or pathogenic outcome. Several AAV serotypes have been tested in clinical gene therapy trials, with AAV2 being the best characterized and most utilized, although several others, including AAV1, an AAV1/2 hybrid, AAV6, AAV8, and AAVrh10, have also been used for clinical study (reviewed in reference 48). AAV vectors exhibit broad tissue tropism, with some able to transduce certain tissues more efficiently than others. For example, AAV8 has repeatedly shown better transduction efficiency compared to other serotype-based vectors in mouse liver (18, 52, 76, 88). The first report of successful treatment of hemophilia A in mice made use of an AAV8 vector (62), and AAV8 has now been used in a human clinical trial to deliver factor IX to hemophilia B patients (54). A comparative study of AAV2, AAV6, and AAV8 vectors in the liver suggested that AAV8 is a more efficient transducer due to rapid uncoating of the viral capsid, which allows for quicker onset of dsDNA production during genome replication (70). This phenotype facilitates 4- to 10-fold higher transduction of mouse liver cells by AAV8 vectors compared to AAV2 (70). However, such high levels of hepatic cell transduction by AAV8-based vectors observed in mice have yet to be repeated in larger animal models. Levels of gene transfer similar to those found in mice have been demonstrated in studies of infant rhesus macaques (73), and recent data suggest lower efficiency in dog models (7). Despite these results, studies in dogs with hemophilia have demonstrated AAV8-mediated continuous expression of canine factor VIIa at levels above normal values (46). These data indicate that even low levels of transduction can produce sufficient amounts of transgene to have a therapeutic effect in a diseased state. However, the presence of neutralizing antibody responses to the AAV capsid are known to efficiently block gene transfer in large animal models (18, 34, 74, 75), as also seen in human patients (45). It has been documented that the human population already has high neutralizing antibody titers to the more common AAV2 (8, 11, 13, 17, 22). In contrast, compared to AAV1, AAV2, AAV5, AAV6, and AAV9, AAV8 is the least seroprevalent (<40%) in humans (11), which highlights the potential usefulness of AAV8 vectors in patients with a preexisting exposure to other serotypes (11, 13). However, high sequence (23) and structural homology (53) among the AAVs and the presence of AAV-reactive antibodies in a large portion of the population (50), make it increasingly difficult to circumvent the detrimental effects of preexisting immunity in gene delivery applications with any AAV vector.

Efforts to study the full impact of preexisting antibody responses on AAV vector delivery are limited by the lack of animal models that adequately recapitulate the natural exposure found in

Received 25 January 2012 Accepted 3 May 2012
Published ahead of print 16 May 2012
Address correspondence to Mavis Agbandje-McKenna, mckenna@ufl.edu.
* Present address: Brittney L. Gurda, Gene Therapy Program, Department of Pathology and Laboratory Medicine, University of Pennsylvania, Philadelphia, Pennsylvania, USA, and Christina Raupp, Physicians World Europe GmbH, Mannheim, Germany.
B.L.G. and C.R. contributed equally to this article.

doi:10.1128/JVI.00218-12

humans. Many studies exploit passive immunity models, in which animals are injected with human-derived "intravenous immunoglobulin" (63, 75). These studies also demonstrated that even low levels of total anti-AAV antibodies, often undetectable levels, can hamper liver transduction (34). Hence, although interest in the use of alternate or newly discovered serotypes to bypass preexisting immune responses is increasing (20, 29), it is important to gain a better understanding of the antigenic structure of AAV capsids. Such insight will aid the selection and engineering of new AAV vectors that can evade the recognition of preexisting antibodies.

The three-dimensional (3D) structures of the capsids of several different AAV serotypes have been determined by X-ray crystallography and by cryo-electron microscopy (cryo-EM) and image reconstruction (cryo-reconstruction) methods (e.g., 26, 43, 53, 55, 57, 82). These structures show that the AAV capsid shell is assembled from 60 copies (in total) of viral proteins (VP), VP1 (~87 kDa), VP2 (~73 kDa), and VP3 (~61 kDa). These proteins share a C-terminal region (~520 amino acids [aa] within VP3) that forms the T=1, icosahedrally symmetric part of the capsid. The N-terminal extension unique to VP1 (aa 1 to 137, VP1u), the VP1/VP2 overlapping amino acids, and ca. 14 to 17 aa of the VP3 N terminus are not observed in any of the structures. The AAV capsid includes 2-, 3-, and 5-fold symmetric interactions among the VP subunits, and these generate characteristic surface features, including depressions at the 2-fold axes, protrusions surrounding depressions at the 3-fold axes, and cylindrical channels at the 5-fold axes surrounded by a depression (reviewed in reference 15). The conserved core of each VP subunit consists of an eight-stranded, β-barrel motif (βB-I) and an α-helix (αA) (15). The outer surface of the capsid is formed by large loops that connect the strands of the β-barrel. These loops are structurally superimposable between the different AAV serotypes and are comprised of nine conformationally variable regions (VRs), designated VRI-VRIX based on comparison of AAV2 and AAV4, which are two structurally diverse serotypes (26). The amino acid sequences and structural topology of these loops are reported to facilitate several important functions, including tissue tropism (involving receptor recognition for internalization and cellular trafficking), transduction efficiency, and the antigenic reactivity directed against the AAV capsid (reviewed in references 1 and 2). Glycan recognition for cell entry has been studied for many of the representative members of the AAV clades, which cluster into three groups: those that bind heparan sulfate (HS; AAV2, AAV3b, and AAV6), those that bind sialic acid (AAV1, AAV4, AAV5, and AAV6), and those that bind galactose (AAV9) (reviewed in reference 2). Glycan receptors have not been identified for AAV7 and AAV8, but for AAV8 the 37/67-kDa laminin receptor (LamR) was reported to play a role in cellular recognition (3). The LamR footprint encompasses amino acids in VRV, VRIV, and VRVIII within the G-H loop (located between the βI and βH strands (3). Residues within the G-H loop were also determined to be critical for AAV8's enhanced liver transduction efficiency compared to AAV2 (65) and a chimera inserting AAV8's VRVIII into AAV2 conferred muscle transduction (4). As for antigenicity, except for AAV2, little is known about specific sequences or surface loop regions of other AAV capsids that interact with antibodies (81).

In this study we identified an antigenic epitope on the AAV8 capsid through structural, genetic, biochemical, and *in vivo* characterization of its interaction with a neutralizing monoclonal antibody (MAb), ADK8 (67). The structure of the AAV8:ADK8 fragment antibody (Fab) complex was determined by cryo-reconstruction methods to 18.7-Å resolution, and a pseudo-atomic model of the structure was built using the available crystal structures of AAV8 (53) and an unrelated Fab (2FBJ [69]). The predicted epitope residues were verified through mutagenesis followed by *in vitro* and *in vivo* transduction assays. Biochemical efforts to characterize the mechanism by which ADK8 neutralizes AAV8 suggest that it does so by acting after cell surface receptor binding and internalization but before entry into the nucleus. Significantly, a mutant AAV8 vector that lacks the confirmed ADK8 epitope can evade neutralization by the ADK8 MAb but retains the liver transduction efficiency of the parental AAV8 vector (C. Raupp et al., unpublished data). This study thus establishes a potentially viable, structure-based strategy that utilizes knowledge about specific regions of the capsid to which host antigenic responses are directed and facilitates the re-engineering of second generation AAV vectors that can escape the surveillance of preexisting host antibodies.

MATERIALS AND METHODS

Animals, cell lines, and cell culture. Nine-week-old, female NMRI mice ($n = 4$ per experiment) were used for all experiments. Mice were purchased from Charles River Wiga (Sulzfeld, Germany) and were maintained according to the guidelines of the German Cancer Research Center. HEK293T (293T) (58), HeLa (laboratory stock), and HepG2 (36) cells were maintained in Dulbecco modified Eagle medium (DMEM) supplemented with 10% heat-inactivated fetal calf serum and 100 U of penicillin/ml and 100 μg of streptomycin at 37°C in 5% CO_2. For transfection, a confluence of 70% of 293T cells was used. For binding assays, HepG2 cells at 90% confluence were used.

Production and purification of MAb ADK8. The generation and basic characterization of MAb ADK8 is described elsewhere (67). To produce sufficient quantities of MAb for purification, hybridoma cells were cultivated with increasing amounts of medium (maximum, 1.5 liters) in expanded surface roller bottles (Sigma-Aldrich, St. Louis, MO) for 12 days. Cells were centrifuged at 4,000 × *g* for 10 min, and the supernatant was collected. For preservation, 0.01% thimerosal was added to the supernatant. The ADK8 MAb was purified from the hybridoma supernatant by affinity chromatography using a protein G-Sepharose column (GE Healthcare Europe GmbH, Munich, Germany). The hybridoma culture was filtered through a 0.45-μm-pore-size filter and applied to the column at room temperature overnight. The column was washed with phosphate-buffered saline (PBS; 137 mM NaCl, 2.7 mM KCl, 100 mM Na_2HPO_4, 2 mM KH_2PO_4 [10 column volumes]), and the antibody was eluted with 10 ml of 0.1 M sodium acetate–0.15 M NaCl (pH 4.4). The eluted antibody was neutralized with 5% 1 M Tris-HCl (pH 9.5). The total MAb yield was determined (Nanodrop ND-1000; Peqlab Biotechnology, Erlangen, Germany) at an optical density of 280 nm.

AAV capture ELISA. The enzyme-linked immunosorbent assay (ELISA) for rAAV8 and mutant virus (generated below) particle titering were carried out using ADK8 MAb (50 ng per well) coated flexible microtiter plates (Becton Dickinson, Heidelberg, Germany). rAAV8 particle titers for the standard were determined by particle counting from random views in 10 electron micrographs of negatively stained samples recorded in a Zeiss EM10 electron microscope. Genome containing particles (10^{10}) were serially diluted and applied to the plates. Horseradish peroxidase (HRP)-labeled (ApD Serotech, Oxford, United Kingdom) ADK8 (1 μg/ml) antibodies were then applied and analyzed by an ELISA plate reader (Ascent FL; Thermo Labsystems, Egelsbach, Germany).

Fab production and purification. For the generation of Fabs from purified ADK8 MAbs, immobilized papain was activated with L-cysteine according to the manufacturer's instructions (Pierce, Rockford, IL) and mixed with purified sample at a suggested enzyme/substrate ratio of 1:160 (wt/wt). The slurry was incubated with moderate shaking at 37°C over-

night. The reaction was stopped with sample buffer (1.5 ml, 10 mM Tris-HCl [pH 7.5]) and then gently centrifuged (200 × *g*, 5 min) to pellet the immobilized papain-agarose beads. The aqueous mixture was carefully removed and diluted in 20 mM sodium phosphate buffer (pH 8.5) and applied to a Hi-Trap protein A column (GE Healthcare, Uppsala, Sweden) using a peristaltic pump at a rate of 1 ml/min. ADK8 Fabs were collected in the flowthrough and concentrated on Amicon-Ultra concentrators (Millipore, Billerica, MA). The Fab samples were then applied to a Superdex 75 10/300 GL (GE Healthcare, Uppsala, Sweden) to verify their size. The purity was monitored by SDS-PAGE.

Preparation of virus-like particles (VLP):Fab complexes. Purified AAV8 VLPs, produced and purified as described by Lane et al. (42), were mixed with Fabs at a ratio of ~2 Fabs per potential VP binding site, assuming that the particles have 60 binding sites, giving a final ratio of ~1:120 (VLP to Fab). Complexes were incubated at 4°C for 1 h and viewed by negative-stain electron microscopy (Sphera; FEI) to visualize Fab decorated virus particles prior to cryo-EM data collection.

Cryo-EM data collection. Sample aliquots of 3.5 μl were vitrified with a manual plunge freezing device on grids with continuous carbon films. The samples were examined at −193°C in an FEI Tecnai G^2 Polara electron microscope at an accelerating voltage of 200 keV and at a nominal magnification of ×59,000. Images were recorded with a Gatan Ultrascan 4000 charge-coupled device (CCD) camera at a step size of 1.883 Å/pixel under low dose conditions (~24 $e^-/Å^2$). All images were recorded with the objective lens underfocused in the range between 1.25 and 3.0 μm.

3D reconstruction of the AAV8:Fab complex. Individual AAV8:ADK8 particle images were extracted from the micrographs using the RobEM software package (http://cryoEM.ucsd.edu/programs.shtm). Preprocessing of the selected images and estimation of the defocus level of each micrograph were performed as previously described (5). The random-model computation procedure (83) was used to generate a starting model of the virus:Fab complex at a ~30-Å resolution from 150 particle images. This map was used to initiate full orientation and origin determination and refinement of the entire set of images with AUTO3DEM (84). Corrections to compensate for the effects of phase reversals in the microscope contrast-transfer function for each micrograph were performed as previously described (12, 87), but amplitude corrections were not applied. The final 3D map, reconstructed from 982 selected particle images, was estimated to be reliable to ~18.7-Å resolution according to the Fourier shell correlation ($FSC_{0.5}$) criterion (data not shown).

Docking of the AAV8 capsid coordinates and scaling of the cryo-EM reconstruction map. The atomic coordinates of the AAV8 capsid (generated from PDB accession number 2QA0 [53]) were docked as a rigid-body into the cryo-reconstructed density map using the COLORES program in the SITUS software package, version 2.3 (14), and was subsequently used to determine the absolute scale (i.e., pixel size) of the cryo-EM map. Scaling of the cryo-EM reconstructed map was done by generating a series of AAV8:ADK8 cryo-reconstructions for a range of different pixel sizes, and each map was compared to an AAV8 map that was generated from the set of structure factors obtained by Fourier transformation of the atomic coordinates of the AAV8 crystal structure. The similarity function in the program MAPMAN (35) was used to compare each reconstructed AAV8:ADK8 density map with the AAV8 model (http://xray.bmc.uu.se/usf/mapman_man.html). The highest correlation coefficient (CC) in this comparison showed that the calibrated cryo-EM map pixel size was 1.90 Å.

The handedness of the cryo-reconstructed AAV8:ADK8 density map was determined by comparison of the surface features with that of the AAV8 capsid determined by X-ray crystallography (53). The most prominent features of the capsid, the protrusions surrounding the icosahedral 3-fold axes, were occluded by the bound Fabs and the CC for the fit of the crystal structure into the density of both hands of the map were comparable at 0.97 and 0.96 (using the "fit in map" command in the program Chimera (http://www.cgl.ucsf.edu/CHIMERA [59]). In addition, difference maps generated in Chimera (using the volume editor command) between the original and "hand-flipped" reconstructed maps and a map generated from a 60-mer of the AAV8 VP crystal structure (PDB accession number 2QA0 [53]), fitted as described above, showed no density differences. Thus, a visual inspection of the AAV8 capsid protrusions in context of the original and flipped maps was utilized to assign the correct hand. In the flipped map, the protrusions were located outside the density envelope. The original reconstructed map was thus interpreted to be of the correct hand and utilized for the interpretation of the Fab footprint. Difference map calculations and CC estimations in Chimera used default values (59).

Epitope mapping. The ADK8 monoclonal sequence is not available. Atomic coordinates for an unrelated (generic) Fab (PDB 2FBJ [69]) was thus used for analysis of its AAV8 capsid epitope. The uninterpreted density following the docking of the AAV8 capsid structure into the reconstructed density of the AAV8-ADK8 and the reconstructed map minus model difference map calculation was interpreted as the bound Fabs. This density was segmented in Chimera using the Segger (v1.6) tool "segment map" (60). Default values were used to generate 243 regions that outlined the complementarity-determining region (CDR) and constant regions of the bound Fab density (data not shown). These segments were used, individually, to fit the CDR and constant domains of the Fab. The "fit-to-segment" option in Chimera (Segger v1.6) was used to fit the Fab structure coordinates into each selected region of the 18.7-Å resolution reconstructed map using a rigid body rotational search. The all atom models of both the CDR and constant domains were fitted with final CCs of 0.98. The "find clashes/contacts" tool was then used, with default parameters in Chimera to analyze the clashes between the CDR and the constant domains, as well as between the CDR and AAV8 capsid monomers. No clashes were observed between the CDR and the constant domain. Contacts between the CDR and amino acids within AAV8 VRIV, VRV, and VRVIII from two VP monomers, visualized the potential ADK8 epitope. AAV8 residue 590 in VRVIII and two CDR residues were observed to be outside of the allowable overlap distance of 0.6 Å; however the docked Fab model was not further manipulated. The PDBePISA server (http://www.ebi.ac.uk/pdbe/prot_int/pistart.html) (38) was used to analyze potential hydrogen bonding interactions and buried surface area (BSA) between the capsid and the docked CDR.

Plasmids and site-directed mutagenesis to verify the ADK8 footprint. Vector plasmid pTRUF2CMV-Luc is a recombinant AAV2 plasmid that expresses a luciferase reporter gene under the control of a cytomegalovirus (CMV) promoter, flanked by inverted terminal repeats (90). Plasmid pDGΔVP expresses all essential Ad helper proteins and AAV2 Rep proteins but does not express AAV VPs (21). The p5E18-VD2/8 helper construct (25) produces AAV2 Rep proteins and AAV8 VPs, and pBSΔTR18 provides AAV2 Rep and VP proteins (77). Both plasmids served as templates for site-directed mutagenesis reactions. The QuikChange site-directed mutagenesis kit (Stratagene, Amsterdam, Netherlands) was used to make mutants in which AAV2 VP amino acids in three AAV VR regions (VRIV, VRV, and VRVIII) were substituted into AAV8 in the proposed ADK8 epitope and AAV8 VRIV and VRVIII residues were substituted into AAV2. For each mutant, two complementary PCR primers were designed that contained the desired substitution, which was flanked on both sides by 10 to 15 homologous base pairs. Three sets of primers were produced and inserted into the *cap* gene of p5E18-VD2/8 (see Table 1). Two sets of primers were produced and inserted into the *cap* gene of pBSΔTR18 (see Table 1). The mutated plasmids were then sequenced to verify that the desired mutations were generated. The recombinant mutant vectors were named to denote the AAV serotype background and the amino acids altered. For example, $rAAV2_{457QSRLQ461 \rightarrow TQTLG}$ refers to the mutant in which AAV2 amino acid residues 457 to 461 (VP1 numbering) were replaced with the sequence TQTLG from AAV8.

Plasmids and peptide insertions to ablate the mapped ADK8 epitope. To insert peptide sequences into the AAV8 VP at the proposed ADK8 epitope, an available SfiI binding site construct (51), produced by synthesizing a fragment of 743 bp (GeneArt, Regensburg, Germany) into

TABLE 1 Primer information for AAV capsid mutagenesis

Template (reference)	Primer		Substitution generated
	Direction[a]	Sequence (5′–3′)	
p5E18-VD2/8 (25)	F	GGAGGCACGACAACTCAGTCGACCCTCTGGGC	456GTANTQ461→GTTTQS
	R	GCCCAGAGTCGACTGAGTTGTCGTGCCTCC	
	F	GCTATTGTTGTTGTCCGCGCTTGTCTTTGAGACGCG	493TTTGQ497→ KTSAD
	R	CGCGTCTCAAAGACAAGCGCGGACAACAACAATAGC	
	F	GCAGATAACTTGCAGC GGGGAAACAGGGCTCCTC	586LQQQNT591→LQRGNR
	R	GAGGAGCCCTGTTTCCCCGCTGCAAGTTATCTGC	
pBSΔTR18 (77)	F	CCAAGTGGAACCACCAATACGCAAACTCTTGGGTTTTCTCAGGC	457QSRLQ461→ TQTLG
	R	GCCTGAGAAAACCCAAGAGTTTGCGTATTGGTGGTTCCACTTGG	
	F	CCACCTCCAGCAACAAAACACAGCGGCAGCTACCGC	585RGNRQ589→ QQNTA
	R	GCGGTAGCTGCCGCTGTGTTTTGTTGCTGGAGGTTGG	

[a] F, forward; R, reverse.

the plasmid p5E18-VD2/8, was used. Oligonucleotides coding for three peptides (VNSTRLP, GQHPRPG, and ASSLNIA [85, 86; Ying et al., unpublished data]) were inserted into the SfiI binding site. The resulting plasmids containing the insertions were verified by sequencing.

Transfection of 293T cells for mutant vector production and vector purification. A triple transfection (with pTRUF2CMV-Luc, pDGΔVP, and either p5E18-VD2/8 or pBSΔTR18) was carried out by calcium phosphate precipitation. For each mutant, 20 plates with 5×10^6 cells each, were seeded, and transfected after 24 h. Per plate, 50 to 60 μg of DNA was resuspended in 1.125 ml of sterile Braun H_2O, mixed with 125 μl of $CaCl_2$ (Sigma, St. Louis, MO) and added slowly to 1.25 ml of 2× HBSS (280 mM NaCl, 50 mM HEPES, 1.5 mM Na_2HPO_4, 10 mM KCl, 12 mM glucose; pH 7.05), while shaking constantly. After 1 min of incubation, the mixture was added to 7.5 ml of medium and applied to the cells. After 48 h of incubation at 37°C, 5% CO_2, the cells were harvested, washed with PBS, centrifuged at 200 × *g* for 15 min, and stored at −80°C until purification was performed.

For purification, 15 ml of a lysis buffer (150 mM NaCl, 50 mM Tris-HCl [pH 8.5]) was added to the cell pellets, followed by five rounds of freeze-thawing (LN_2 and 37°C), 30 min of benzonase (50 U per ml) treatment at 37°C, and a 15-min spin at 3,000 × *g* to collect the cell lysate. The virus particles were purified from the cell lysate using a 15 to 60% iodixanol step-gradient (89). Sealed gradient tubes (Beckman) were centrifuged at 50,000 × *g* at 4°C for 2 h. Virus particles were aspirated from the 40% iodixanol phase and frozen at 20°C until further use. Quantification of AAV with packaged genome was achieved by quantitative real-time PCR adapted from a previously described method (72). After the alkaline lysis of the AAV particles, genomes were subjected to a TaqMan Universal Master mix including primer (for-5′-TGCCCAGTACATGACCTTATG G-3′ and rev-5′-GAAATCCCCGTGAGTCAAACC-3′) and probe (6-fam-AGTCATCGCTATTACCATGG-MGB) and analyzed under standard quantitative reverse transcription-PCR conditions (Applied Biosystems, Inc., Foster City, CA).

Analysis of viral protein expression. To check the expression level of wild-type (wt) and mutant viruses, Western blot analysis was performed with equal amounts of genome containing particles according to standard methods (33). MAbs were applied as previously described (81).

***In vitro* and *in vivo* neutralization.** HepG2 cells in fetal calf serum (FCS)-free medium were seeded onto 96-well plates (Nunc, Rochester, NY) 24 h prior to infection. The rAAV8, rAAV2, and the $rAAV2_{585RGNRQ589\rightarrow QQNTA}$ viral particles, at a multiplicity of infection (MOI) of 5×10^4, were preincubated with 0, 250, or 500 ng of antibodies ADK8 and A20 (specific for AAV2) for 30 min at 37°C and added to the HepG2 cells. After 4 h, the medium was aspirated, cells were washed with PBS, and DMEM+FCS was added. After 72 h the medium was aspirated, the cells were washed with PBS and 1× RLB (reporter lysis buffer; Promega GmbH, Mannheim, Germany) was applied. Cell extracts were stored at −80°C until expression analysis was performed.

For the *in vivo* studies, mice were injected intraperitoneally (i.p.) with 0, 50, or 250 μg of MAb ADK8 or 250 μg of MAb ADK4 (specific for AAV4) 4 h prior to intravenous injection with 10^{11} genome (luciferase gene) containing rAAV8 viral particles. Fourteen days after the injection, the animals were injected with D-luciferin (30 mg/ml; Synchem OHG, Altenburg, Germany) and analyzed by the IVIS Imaging software (Xenogen, Alameda, CA) for 5 min (10 min after the D-luciferin injection). The mice were sacrificed, and the liver and heart were extracted to assay for the level of transgene expression using a luciferase reporter assay. The amount of protein was determined with a NanoOrange protein quantification kit (Invitrogen, Karlsruhe, Germany).

Immunofluorescence analysis of AAV8 cell binding in the presence of ADK8. HeLa cells were seeded onto coverslips in 24-well plates (7×10^4 cells/well) 24 h prior to infection. rAAV8 particles (MOI of 10^6) were preincubated with 0.1 mg of ADK8 or IVA7 (none AAV8 specific laboratory MAb stock) at 37°C for 30 min then on ice for 10 min. The virus-antibody mix was added to precooled coverslips and kept at 4°C for 30 min. As negative controls, ADK8 alone or buffer alone was added. As a positive control, virus alone with no antibody was added. Cells were washed with PBS and directly fixed with ice-cold methanol for 10 min and washed again with PBS. After fixation, ADK8 hybridoma culture was applied overnight. The cells were then washed three times for 10 min each time with PBS and kept at room temperature for 1 h in the dark after the secondary goat anti-mouse Alexa-Fluor 488 antibody (Dianova GmbH, Hamburg, Germany), diluted 1:700 in PBS–1% BSA, was applied. Finally, coverslips were washed twice with PBS and mounted with Permafluor mounting medium on glass slides for viewing. Examination was carried out with a fluorescence microscope (Leica DMRD).

Immunofluorescence analysis of AAV8 intracellular trafficking. For analyzing AAV8 intracellular trafficking in the presence of MAb ADK8, HeLa cells were seeded onto coverslips (24-well plate, 7×10^4 cells/well) and grown for 24 h in DMEM supplemented with 10% FCS, 1% glutamine, and 1% penicillin-streptomycin (DMEM-c). Prior to infection, purified rAAV8 particles were incubated with 500 ng of purified MAbs ADK8 or ADK4 (control antibody) or PBS (no antibody) at 37°C for 30 min. rAAV2 was used as a negative control with PBS and ADK8. The cells were infected with the respective virus alone or antibody-preincubated virus at an MOI of 2×10^5 genome containing particles. After incubation at 37°C for 1 h in DMEM with 50 mM HEPES buffer (Sigma) and 2 μM MG132 (proteasome inhibitor), the viruses were removed, and the cells were further cultivated in DMEM-c with 2 μM MG132. At the indicated time points postinfection, cells were fixed with 2% paraformaldehyde at room temperature for 15 min, followed by quenching of free aldehyde groups with 50 mM NH_4Cl/PBS (two times for 5 min each time, room temperature) and membrane permeabilization with 0.2% Triton X-100/PBS (10 min, room temperature). After several washing steps with PBS, the cells were incubated with blocking solution (PBS, 1% BSA) at room tem-

perature for 30 min. For immunodetection, virus particles were stained with either purified ADK8 (AAV8; Progen, 1:2,500) or A20 hybridoma supernatant (AAV2; lab stock, undiluted) and a chicken anti-mouse secondary antibody coupled to Alexa 488 (green) (Molecular Probes, 1:1,000). Nuclei were visualized with anti-Lamin B (Santa Cruz; 1:200) and chicken anti-goat secondary antibody coupled to Alexa 594 (red) (Molecular Probes, 1:700) staining. Coverslips were mounted onto glass slides with PermaFluor (Thermo Fisher Scientific) mounting medium. Confocal images were taken with a Zeiss LSM 710 ConfoCor3 using a 63× oil immersion objective. Images were optimized for printing with ImageJ software.

DNA dot blot analysis of cell binding in the presence of ADK4 and ADK8. HepG2 cells were seeded out on six-well plates 24 h prior to infection. Viral particles of rAAV8, rAAV2, and the $AAV2_{585RGNRQ589\rightarrow QQNTA}$ mutant (MOI of 5×10^4) were preincubated with 0, 250, or 500 ng of antibody (ADK8 and ADK4) for 30 min at 37°C. After incubation, the virus-antibody mixture was shifted to 4°C before being applied to the cells (also at 4°C) for 30 min. The cells were washed with PBS and either harvested or shifted to 37°C for 2 h after addition of DMEM and then harvested. Infected cells not shifted to 37°C were centrifuged at 200 × *g* for 10 min, and the medium was aspirated. The temperature-shifted samples were centrifuged, the medium was aspirated, 100 μl of prewarmed trypsin (0.05%) was added for 5 min, followed by additional centrifugation, and then the medium was carefully removed. Cell pellets were stored at −20°C until further processing. For DNA dot blots, the cells were treated with nuclease (1 mg/ml) and proteinase K (10 mg/ml) (Roche, Pensberg, Germany), followed by phenol-chloroform extraction of the DNA. The DNA samples were spotted onto a nylon membrane (GeneScreen; DuPont, Boston, MA) in a dot blot chamber, denatured for 10 min (in 1.5 M NaCl, 0.5 M NaOH), neutralized for 10 min (in 0.5 M Tris-HCl [pH 7.0], 0.3 M Tris-sodium citrate, 3 M NaCl), and UV-cross-linked at 1,200 J. A radioactive probe, directed against CMV, was produced with the standard protocol from a DNA labeling kit (Roche) and 5 μl of [α-^{32}P]dCTP (50 μCi). On the nylon membrane, immobilized template DNA was prehybridized in 15 ml of hybridization buffer (125 mM Na_2HPO_4, 250 mM NaCl, 1 mM EDTA, 45% formamide, 7% SDS), probe was added, and the DNA was labeled in a hybridization oven at 42°C overnight while being rotated. The membrane was washed six times for 5 min each time with wash buffer I (2× SSC, 0.1% SDS) at 42°C and three times for 20 min each time with wash buffer II (0.1× SSC (150 mM NaCl, 15 mM Tri-sodium citrate [dihydrate; pH 7.0], 0.1% SDS) at 68°C. The membrane was then exposed to an X-ray film (Kodak BioMax MS; Sigma). The pixel intensities for each spot were analyzed by the ImageJ software (http://rsbweb.nih.gov/ij/).

Native Western dot blot assay to assess VP1u externalization in the presence of ADK8. Wild-type and mutant viruses (rAAV2, rAAV8, and $AAV2_{585RGNRQ589\rightarrow QQNTA}$) in PBS were incubated at 37°C for 30 min without or with ADK8 (2 mg/ml) and then for 10 min on ice. Next, the samples were subjected to a temperature treatment, 37, 65, or 71°C for 5 min. Samples were spotted on a nitrocellulose membrane (Schleicher & Schuell, Dassel, Germany) in a dot blot chamber. The membrane was blocked in PBS–10% skimmed milk powder and incubated with the AAV2 A1 antibody (epitope located at the VP1u [80, 81] of the AAVs) and visualized with purified A1 directly linked to HRP (Zenon labeling kit; Invitrogen). Particle visualization was performed using an enhanced chemiluminescence detection kit (Perkin-Elmer, Boston, MA).

Native Western dot blot of AAV8-ADK8 complexes incubated at pH 5.2. Wild-type rAAV8 particles (3×10^{10}) were spotted onto a nitrocellulose membrane and incubated with ADK8 and then exposed to an acidic solution (sodium acetate-acetic acid buffer solution [pH 5.2]) for 0.5, 1, 2, and 4 h. After several washes with PBS, AAV8 particles were detected by a secondary goat anti-mouse antibody conjugated to HRP and visualized as described above.

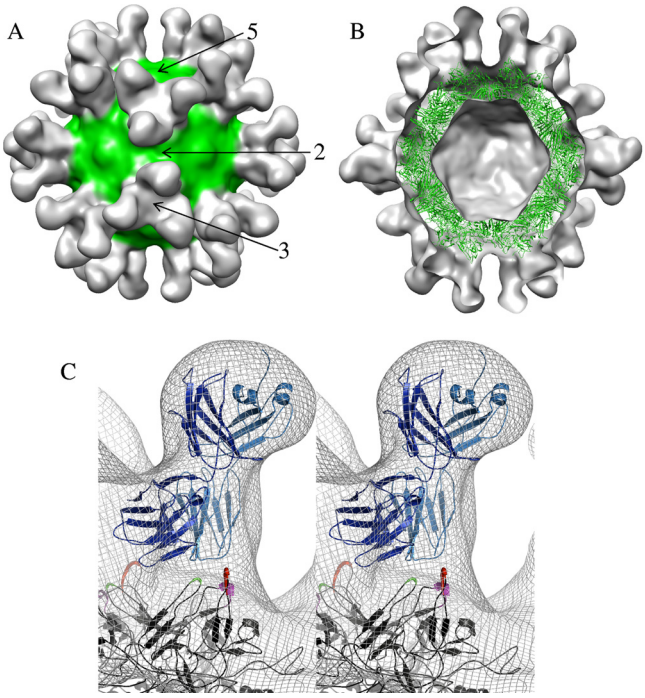

FIG 1 3D cryo-reconstruction and pseudo-atomic model of the AAV8:ADK8 complex. (A) Shaded-surface representation of the 18.7-Å resolution AAV8:ADK8 reconstruction, viewed along a 2-fold axis of symmetry. The AAV8 capsid and Fab density are colored green and gray, respectively. (B) A central slab from the AAV8:ADK8 density map to which a 60mer of the AAV8 VP3 crystal structure (RCSB PDB accession no. 2QA0) was fitted (density map in gray and atomic coordinates in green). The unassigned density is attributed to the bound Fab molecules. (C) Stereo view close-up of a portion of the pseudo-atomic model of the AAV8:ADK8 complex built into the reconstructed density map (gray mesh). One Fab molecule (heavy chain shown in dark blue and light chain in sky blue; PDB 2FBJ) lies above the docked coordinates for two 3-fold symmetry-related AAV8 VP3 monomers (in black and light gray), which form one of the three protrusions around each icosahedral 3-fold axis. The capsid VR regions in contact with the Fab molecules are shown in red (VRIV), purple (VRV), and green (VRVIII).

RESULTS AND DISCUSSION

3D reconstruction and model of the AAV8:ADK8 complex. A total of 982 particles were boxed from 78 CCD images to generate a final 3D reconstruction of the AAV8:ADK8 complex to an estimated resolution of 18.7 Å (Fig. 1A). This modest resolution density map was useful for the docking of capsid and Fab atomic coordinates and subsequent evaluation of capsid regions important for the Fab interaction. The density map of the virus:Fab complex is consistent with the known structure of the AAV8 capsid that is decorated with a full complement of 60 Fab molecules, with the Fab density visible at the same sigma threshold as the capsid, indicating a saturation of binding sites. The density attributed to each Fab extends from the protrusion that surrounds each icosahedral 3-fold symmetry axis of the capsid and leaves unobstructed the surface of the capsid at each 2- and 5-fold axis (Fig. 1A). A pseudo-atomic model of the virus:Fab complex was constructed based on fitting atomic models of AAV8 (residues 220 to 738 ordered in the crystal structure [53]) and a generic Fab (69) into a scaled cryo-EM map (Fig. 1B and C; see also Materials and Methods). A generic Fab structure was used because there is no sequence information available for the ADK8 antibody. Also, the

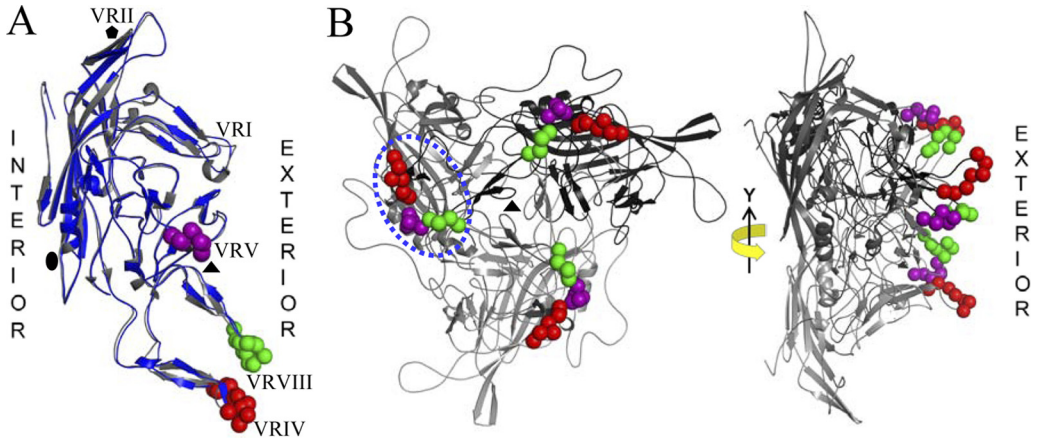

FIG 2 Structural comparison of the AAV2 and AAV8 VP monomers. (A) AAV8 VP structure (2QA0; colored gray [53]) superimposed onto that of the AAV2 VP (PDB ID 1LP3; blue [82]) with the predicted ADK8 within VRIV, VRV, and VRVIII (as defined in references 26 and 53) shown in red, purple, and green spheres, respectively. Variable regions I and II are labeled; the approximate location of icosahedral 2-, 3-, and 5-fold axes are indicated by a filled oval, triangle, and pentagon, respectively. Regions of the VP contributing to the interior and exterior of the capsid are indicated. (B) A trimer of the AAV8 VP structure viewed approximately down the icosahedral 3-fold axis (filled triangle; left) and rotated 90° (right) with VRIV, VRV, and VRVIII depicted as in panel A. The dashed oval (blue) encircles one of the three protrusions surrounding the icosahedral 3-fold created by two symmetry-related VP monomers (dark gray and black) to highlight the structural juxtaposition of VRIV and VRVIII from one VP monomer (black) and VRV from another (dark gray).

N-terminal regions of the AAV VPs have not been observed in any of the crystal structures determined to date, and thus could not be modeled reliably in a low-resolution cryo-reconstruction. The atomic structures of the AAV8 VP3 and generic Fab were docked using a rotational rigid-body approach, which does not properly model conformational changes that may have occurred in either structure as have been seen in other antibody-antigen complexes (19). Thus, the atomic clash observed between two Fab CDR amino acids and AAV8 residue 590 in VRVIII, following the docking of the Fab structure, would be expected to be resolved by side chain shifts which cannot be modeled at the resolution of the complex structure.

Pseudo-atomic model of the AAV8-ADK8 complex predicts potential antibody contact regions. The pseudo-atomic model of the AAV8:ADK8 complex (Fig. 1C) provided a means to predict the location of the ADK8 binding site on the AAV8 capsid. Inspection of the virus:Fab model identified amino acids within three VRs—VRIV, VRV, and VRVIII (defined in reference 26)—as the most probable sites for ADK8 interaction. These correspond to peptides 456-GTANTQ-460 (in VRIV; VP1 numbering), 493-TTTGQNNNS-501 (in VRV), and 586-LQQQNT-591 (in VRVIII) (Fig. 2). These VRs form the top of the protrusions that surround the 3-fold axes (53). VRIV and VIII are contributed by one VP monomer and VRV maps to a 3-fold symmetry-related VP. Analysis of the model interfaces using PDBePISA (38) highlighted residues 589 to 591 in VRVIII as likely to form hydrogen bond interactions at distances of 3.07 to 3.84 Å with the Fab CDR residues. Interestingly, the VRVIII peptide has been described as a $H2^k$ MHC II-restricted-epitope (16). Also of note, these regions include residue repeat patterns. For example, VRV and VRVIII both have three residue stretches of hydrophilic, polar residues, such as TTT, NNN, and QQQ. The BSA (calculated in PDBePISA) based on the AAV8-Fab pseudo-atomic model was ~405 $Å^2$ between the interface atoms in the 3-fold protrusion and the fitted generic Fab structure. This value is lower than footprints reported for other antigen-antibody complexes, which are generally between 680 and 800 $Å^2$ (78, 79). The low BSA may be due to the limited surface provided by the protrusion that forms the epitope, specificity resulting from affinity maturation, or the rigid body docking of the Fab that minimized clashes. The surface area of the AAV8 capsid occluded by the Fab density is larger than the calculated BSA and creates a footprint similar to those for other antibody contacts.

Recombinant AAV8 (rAAV8) and rAAV2 capsid mutants pinpoint the important ADK8 binding epitope. The ADK8 epitope on the AAV8 capsid was verified with chimeric, recombinant capsid mutant constructs with residue exchanges within VRIV, VRV, and VRVIII between AAV8 and AAV2. AAV2 was chosen as the serotype for these chimeric mutations for three reasons: (i) its backbone structure is similar to AAV8, which could minimize the effects of substitution mutations on capsid assembly compared to random mutations; (ii) it does not cross-react with ADK8; and (iii) the available A20 MAb (specific for AAV2) provided an additional reagent for characterizing the mutants. The amino acids exchanged were based on a sequence and structure alignment of the VRs in AAV2 and AAV8 (data not shown).

As determined by quantitative real-time PCR (level of genome packaging), the wt rAAV2 and rAAV8 vectors, as well as four of the five mutant viruses ($rAAV2_{457QSRLQ461→TQTLG}$, $rAAV2_{585RGNRQ589→QQNTA}$, $rAAV8_{456GTANTQ461→GTTTQS}$, and $rAAV8_{493TTTGQ497→KTSAD}$), had comparable virus titers (Fig. 3A). The $rAAV8_{586LQQQNT591→LQRGNR}$ mutant showed a 20-fold decrease in yield (Fig. 3A). The reduction in yield observed for this mutant maybe due to differences in interactions between the amino acids that make up their VRVIII region. Despite similarities in their backbone structures, side chain interactions within this loop and between the loop residues and the adjacent VRIV and VRV differ between the viruses. When VRVIII of AAV2 is inserted into AAV8, weak side chain interactions between Q589 at the top of the 3-fold protrusion with VRIV and VRV residues are lost, which may result in a lowered capsid production. Interestingly, the reverse mutation, $rAAV2_{585RGNRQ589→QQNTA}$ (VRVIII of AAV8 inserted next to VRV of AAV2), is supported (Fig. 3A). In this mutation the side chain for the substituted Q589 position has the potential to interact with VRV amino acids to

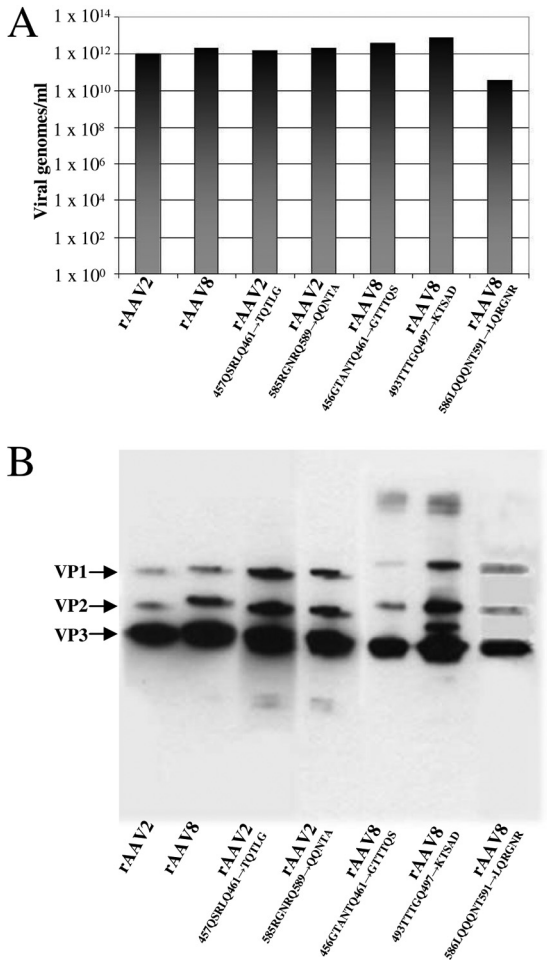

FIG 3 Titers of rAAV2 and rAAV8 substitution mutant vectors. (A) Quantitative real-time PCR analysis (qPCR) data for the wt and mutant viruses as labeled. With the exception of the rAAV8$_{586LQQQNT591→LQRGNR}$ mutant, all others showed comparable packaging capacity to the wt rAAV2 and rAAV8 viruses. Mutant rAAV8$_{586LQQQNT591→LQRGNR}$ showed a 20-fold decrease compared to the wt titers. Each bar represents an average of data from two assays. (B) Western blot analysis of VP protein expression. Analysis with the B1 antibody (directed at the C terminus common to all three capsid VPs) (81) showed the presence of VP1, VP2, and VP3 (arrows) at the expected stoichiometry of ~1:1:10 for the wt and mutant viruses. The rAAV8$_{493TTTGQ497→KTSAD}$ mutant showed an additional VP band migrating between VP2 and VP3. The origin of this protein is yet to be determined.

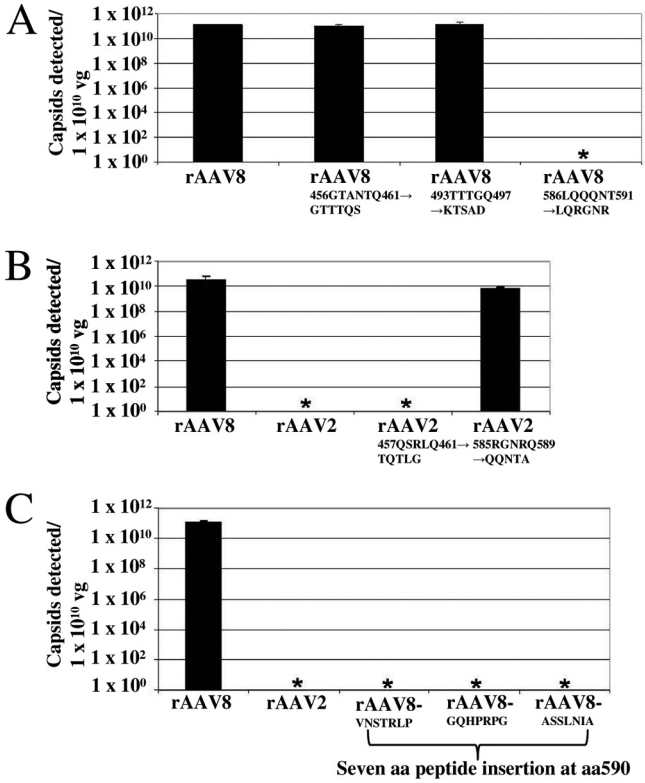

FIG 4 Recognition of wt rAAV2, rAAV8, and their chimeras by ADK8. (A) ADK8 ELISA for rAAV8 and rAAV8 with AAV2 amino acid substitution mutants. Wild-type rAAV8 and the mutants rAAV8$_{456GTANTQ461→GTTTQS}$ and rAAV8$_{493TTTGQ497→KTSAD}$ were detected by the ADK8, but the rAAV8$_{586LQQQNT591→LQRGNR}$ mutant was not. (B) ADK8 ELISA for rAAV2, rAAV8, and rAAV2 with AAV8 amino acid substitution mutants. Wild-type rAAV2 and the rAAV2$_{457QSRLQ461→TQTLG}$ mutant were not recognized by ADK8, but the rAAV2$_{585RGNRQ589→QQNTA}$ mutant was. (C) ADK8 ELISA for rAAV8 and seven-residue peptide insertion (at aa 590) mutants. All insertions disrupted AAV8 detection by ADK8. In panels A to C, the mean standard deviations from four independent experiments are shown; asterisks identify mutants for which capsids could not be detected in the ADK8 ELISA (detection limit, 10^8 capsids/ml). A total of 10^{10} viral genomes were used for each ELISA.

impart stability. Viral protein expression was not impaired for any of the mutants, as indicated by the characteristic banding pattern of VP1, VP2, and VP3 observed in the Western blot (Fig. 3B). An extra VP protein band was observed between VP2 and VP3 for the rAAV8$_{493TTTGQ497→KTSAD}$ mutant and a slower-migrating VP1 (compared to the wt) was observed for rAAV8$_{456GTANTQ461→GTTTQS}$ and rAAV8$_{493TTTGQ497→KTSAD}$ (Fig. 3B). Residue type and subsequent charge changes may have resulted in a difference in the VP degradation pattern for rAAV8$_{493TTTGQ497→KTSAD}$ and in the interaction of VP1 with SDS leading to increased retardation. The observation that the recombinant mutant capsids assembled efficiently around the packaged genome is consistent with the comparison of the crystal structures of AAV2 and AAV8, which showed that they are very similar overall and exhibit significant conformational differences only in VRI, VRII, and VRIV (53). The VRIV difference, located at the top of the protrusions, is not involved in any intra- or intersubunit interactions and, as such, the rAAV8$_{456GTANTQ460→GTTTQS}$ mutant assembled into particles at the same level as the wt AAV8.

Binding of ADK8 antibody to AAV2, AAV8, and the five chimeric AAV2/AAV8 mutants was tested by an ADK8 ELISA. For the rAAV8→rAAV2 sequence change mutants, particles of rAAV8$_{456GTANTQ461→GTTTQS}$ (VRIV) and rAAV8$_{493TTTGQ497→KTSAD}$ (VRV) were detected at the same levels as that for wt rAAV8 (Fig. 4A). Of note, the ELISA results showed that 10-fold more capsids were detected than the viral genome containing particle amount (1^{10}) used in the assay (Fig. 4A). This finding is consistent with a previous report that showed 10- to 100-fold higher amounts of capsids are normally present in samples that have been purified using a single iodixanol step-gradient compared to the genome titers obtained from cell lysates (30). In contrast to the mutants with changes in VRIV and VRV, the third mutant, rAAV8$_{586LQQQNT591→LQRGNR}$, was not detected with the ADK8-ELISA. Hence, the 586-LQQQNT-591 peptide was identified as

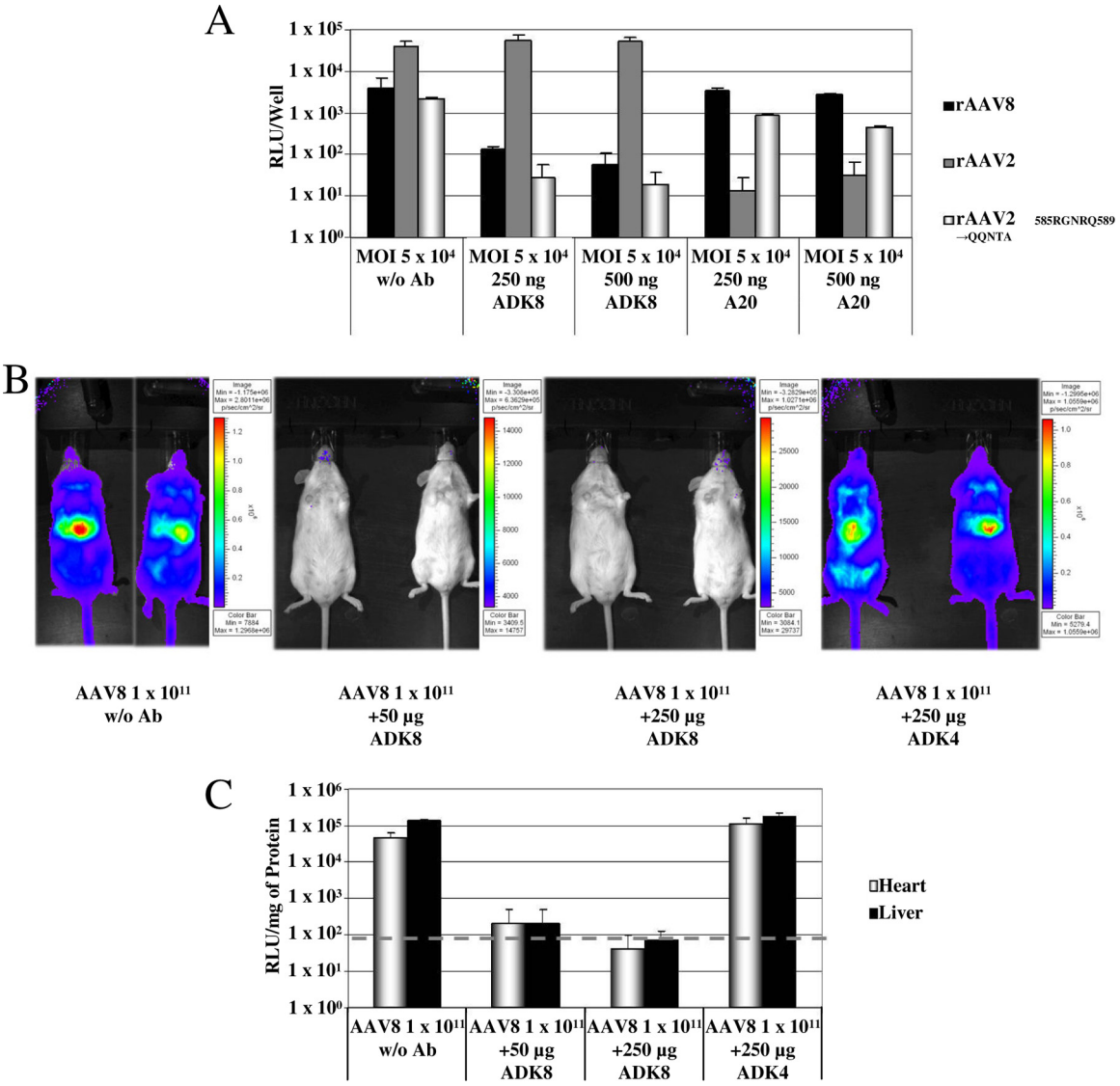

FIG 5 *In vitro* and *in vivo* neutralization of rAAV8 gene transduction by ADK8. (A) Histogram of luciferase reporter gene expression, quantified as relative light units (RLU, *y* axis), following HepG2 cell infection by rAAV8, rAAV2, and rAAV2$_{585RGNRQ589\rightarrow QQNTA}$ in the presence of ADK8 and A20 (specific for AAV2). The amounts of antibody used for virus preincubation—0, 250, and 500 ng—prior to infection are indicated for each virus. The virus color keys for the histograms are shown to the right hand side. (B) Luciferase expression in NMRI mice infection with rAAV8 (intravenous injection) after i.p. injection of ADK8 (50 or 250 µg) or ADK4 (250 µg) 4 h prior to infection. The data show reporter gene expression for 2 weeks postinfection. (C) Quantification of *in vivo* luciferase expression, expressed as RLU/per mg of protein, in the hearts and livers of sacrificed mice. The dashed line indicates the detection limit of the luciferase reporter assay.

being important for ADK8 binding to rAAV8 (Fig. 4A). This result was substantiated by the second set of mutants in which AAV8 residues were substituted into AAV2. The rAAV2$_{457QSRLQ461\rightarrow TQTLG}$ mutant could not be detected by the ADK8 ELISA, but the rAAV2$_{585RGNRQ589\rightarrow QQNTA}$ mutant was detected (Fig. 4B). Additional mutagenesis experiments, in which seven-residue-long insertions were introduced at position 590 of rAAV8, further corroborated evidence that VRVIII residues in AAV8 are required for ADK8 to bind. These insertions completely abolished the detection of capsids in the ADK8 ELISA for all mutants tested (Fig. 4C). Taken together, the results of the VR swaps and insertional mutagenesis experiments demonstrated that, of the three potential binding sites predicted by the AAV8-ADK8 pseudo-atomic model, residues 586-LQQQNT-591 are directly involved in ADK8 binding to AAV8.

ADK8 can neutralize AAV8 infection *in vitro* and *in vivo*. To gain insight into the basis of AAV8 neutralization by ADK8, the impact of this antibody on *in vitro* and *in vivo* transduction efficiency (as measured by luciferase expression) was evaluated (Fig. 5). *In vitro*, ADK8 decreased transduction efficiency for wt AAV8, as well as the rAAV2$_{585RGNRQ589\rightarrow QQNTA}$ mutant (recognized by ADK8), by >50-fold at the two antibody levels (250 or 500 ng) used compared to vector transduction without added antibody (Fig. 5A). However, ADK8 did not neutralize AAV2 (Fig. 5A), a finding consistent with the absence of the epitope sequence in this virus. Viruses preincubated with A20, a MAb specific for AAV2, almost completely neutralized AAV2 transduction but had no influence on AAV8 transduction (Fig. 5A). This indicates that AAV8 does not contain the sequence responsible for A20 binding to AAV2. This is consistent with the proposed A20 epitope

(AAV2 residues 272 to 281, 369 to 378, and 566 to 575, as proposed by Wobus et al. [81], and at positions 263, 264, 384, 385, 548, and 708, as proposed by Lochrie et al. [44]) being located at or close to VRs where AAV2 and AAV8 differ either in sequence or structure (53). The transduction efficiency for mutant rAAV2$_{585RGNRQ589\rightarrow QQNTA}$ was slightly reduced by A20, which is consistent with its epitope still being present in the parental AAV2. The reduction in transduction efficiency for this mutant suggests that the substitution of AAV2 VRVIII residues with those from AAV8 VRVIII alters the A20 binding site even though the residues do not overlap with the A20 epitope identified by others (81). However, residues 573 to 575, within the 566-575 peptide proposed as part of the A20 epitope, are located adjacent to residues 582 and 583 in the VP loop containing VRVIII at its top in a 3-fold symmetry-related VP monomer. Thus, it is plausible that mutations in VRVIII indirectly affect the contact between A20 due to the proximity of its binding site to this loop and the substituted VRVIII residues.

For the *in vivo* studies, mice not injected with antibody exhibited a typical imaging pattern for a hepatotropic AAV vector (Fig. 5B) (62). The lowest amount of ADK8 used, 50 μg, was sufficient for complete neutralization of rAAV8 vector transduction (Fig. 5B). Injection with non-AAV8 MAb ADK4 did not affect AAV8 mediated gene expression (Fig. 5B). The imaging results were verified by a reporter expression analysis of liver and heart after dissection of the animals (Fig. 5C). As observed in the imaging studies, luciferase reporter expression was reduced more than 100-fold in liver and heart after i.p. injections containing 50 μg of ADK8. The number of relative light units (RLU) measured fell below the detection limit after an i.p. injection of 250 μg of ADK8. Injection of 250 μg of ADK4 also had no impact on luciferase reporter expression levels (Fig. 5C). The level of transduction efficiency with this non-AAV8 specific antibody was the same as rAAV8 transduction without prior antibody injection. Combined with the *in vitro* data, these *in vivo* observations are consistent with the neutralization effects of ADK8 on rAAV8 and rAAV2$_{585RGNRQ589\rightarrow QQNTA}$ transduction being due to specific recognition via the 586-LQQQNT-591 epitope and abrogation of a specific function rather than the mere presence of antibody.

Mechanism of ADK8 neutralization. Antibodies are capable of neutralizing virus infection at various steps in the viral life cycle. This includes cell surface receptor binding, virus internalization/entry, endosomal trafficking and release, or capsid uncoating. To identify the point at which ADK8 neutralizes AAV8 infection, cell binding by AAV8, as well as intracellular trafficking in the absence or presence of ADK8 or control antibodies (IVA7 or ADK4), was analyzed by immunofluorescence, and cell binding was also monitored by a DNA dot blot. In addition, cellular uptake, endosomal trafficking, and externalization of the VP1 N termini upon heat treatment (which mimics the capsid/VP transition required to escape the endocytic pathway) (9, 39) in the presence of ADK8 were monitored by DNA dot blot and Western blot tests, respectively.

The ADK8 MAb did not prevent rAAV8 vectors from binding to HeLa cells (Fig. 6A). Particles of rAAV8 complexed with ADK8 bound to the cell surface in a similar manner to rAAV8 alone or AAV8 preincubated with the unrelated IVA7 MAb. The control (noninfected) cells were not decorated with virus particles. In cellular trafficking studies, HeLa cells infected with rAAV8 in the absence of antibody or in the presence of the nonspecific ADK4

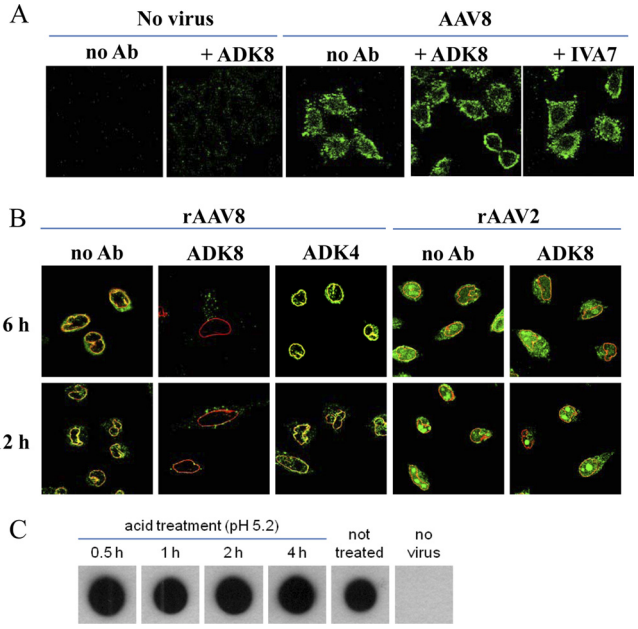

FIG 6 Cell binding and intracellular trafficking of rAAV8 in the presence of ADK8. (A) Wide-field image of HeLa cells infected with AAV8 alone or after preincubation with ADK8 or a nonspecific IVA7 MAb. Cells treated with PBS (no Ab) or with ADK8 alone are also shown. rAAV8 was visualized with ADK8 and secondary goat anti-mouse Alexa Fluor 488 (green) antibody. (B) Confocal image of HeLa cells infected with rAAV2 or rAAV8 alone or after incubation with antibodies ADK8 or ADK4 in the presence of 2 μM proteasome inhibitor MG132. The images show the localization of virus and the nuclei at various time points. rAAV8 was stained with ADK8/Alexa Fluor 488 (green) and AAV2 was stained with A20/Alexa Fluor 488 (green); nuclei were visualized with anti-lamin B/Alexa Fluor 594 (red) staining. Regions where virus and nuclei colocalize appear yellow. Confocal images were taken using a 63× oil immersion objective lens. (C) Native Western dot blot of rAAV8 incubated with ADK8 for the time points indicated at pH 5.2 or left at physiological pH and detected by secondary antibody conjugated to HRP. The reactivity for the treated samples was comparable to that of the untreated samples.

MAb showed robust nuclear membrane accumulation by 6 h and some nuclear entry by 6 and 12 h (Fig. 6B). Entry of rAAV2 into HeLa cell nuclei increased at 6 h with or without preincubation with ADK8 prior to infection (Fig. 6B). The apparent lower level of rAAV8 nuclear entry and accumulation in the absence antibody compared to rAAV2 correlates with previous observations of low transduction levels for the former vector *in vitro* (31). In stark contrast, preincubation of rAAV8 with ADK8 resulted in a significant decrease in the number of virus particles in the cytoplasm and a complete loss of nuclear membrane association and nuclear entry (Fig. 6B). These results thus suggested that ADK8 neutralization of AAV8 likely involved inhibition of a step that follows cell attachment that may be required for cellular entry and/or endocytic pathway trafficking to the nucleus. Native capsid dot blot experiments verified the stability of the AAV8-ADK8 complex under endosomal conditions. Incubation of the complex for different time points at pH 5.2, followed by neutralization and secondary antibody detection, showed that the antibody complex is stable under these conditions (Fig. 6C). Thus, the inhibition of intracellular trafficking by ADK8 is not due to altered AAV8 capsid stability and the ADK8 remains bound to the capsid under these conditions.

DNA dot blot analysis performed with HepG2 cells confirmed

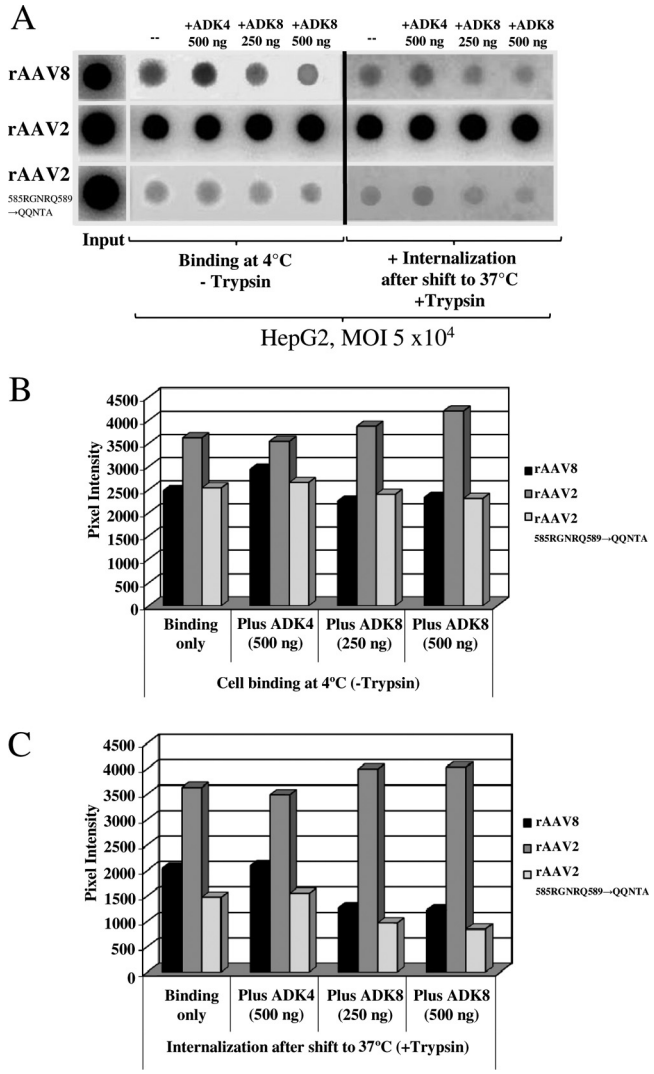

FIG 7 (A) Cell binding and internalization by rAAV8 in the presence of ADK8. (A) DNA dot blot analysis of rAAV2, rAAV8, and $rAAV2_{585RGNRQ589\rightarrow QQNTA}$ binding to HepG2 cells without antibody and in the presence of ADK8 and nonspecific ADK4. The data correspond to cell binding at 4°C (left side) and entry after cells were transitioned to 37°C and then treated with trypsin to remove noninternalized viral particles (right side). The positive control was the viral load without cell infection. The data shown are for one of three independent experiments. (B) Pixel intensities of DNA genomes in viral particles that bound to cells at 4°C. (C) Pixel intensities of DNA genomes in particles that entered the cells at 37°C.

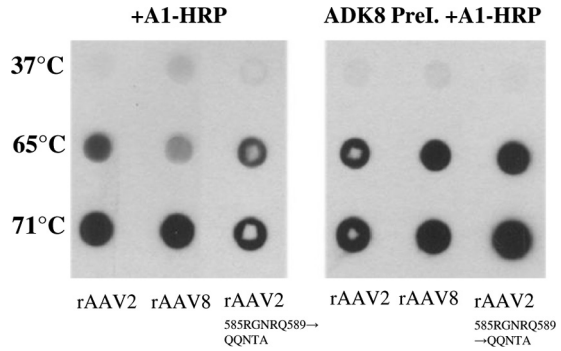

FIG 8 Impact of ADK8 on VP1u externalization after heat treatment. Native Western dot blots for rAAV2, rAAV8, and $rAAV2_{585RGNRQ589\rightarrow QQNTA}$ in the absence (left) or presence (right) of ADK8 detected with the A1-HRP antibody (directed against VP1u) after heat treatment at 37, 65, and 71°C. VP1u externalization from the capsid was not hampered by ADK8 binding. In contrast, its exposure is increased in the presence of ADK8 at 65°C.

the cell binding data obtained by immunofluorescence and suggested that ADK8 slightly impairs AAV8 internalization (Fig. 7). The same amounts of rAAV8 and $rAAV2_{585RGNRQ589\rightarrow QQNTA}$ vector genomes (equated to the number of bound particles) were associated with HepG2 cells infected at 4°C with or without ADK8 preincubation (Fig. 7A [left side] and B). Internalization of bound virus particles, measured following a temperature shift to 37°C and trypsin treatment to remove virus still attached to the cell surface, showed an ~35% reduction in the number of internalized rAAV8 and $rAAV2_{585RGNRQ589\rightarrow QQNTA}$ vector genomes after preincubation with ADK8 (Fig. 7A, right side, and C). In contrast, rAAV2 binding and internalization were not reduced by ADK8, but instead showed a marginal enhancement of ~13% (Fig. 7B and C). The level of rAAV2 cell binding and entry exceeded that of rAAV8, which correlated with the immunofluorescence images (Fig. 6B and 7B and C). The ADK4 antibody did not reduce vector uptake for any of the tested viruses. These data show that ADK8 has a small negative impact on rAAV8 and $rAAV2_{585RGNRQ589\rightarrow QQNTA}$ cellular entry and, as shown by immunofluorescence, ~65% of the bound viruses that are able to enter the cell are impaired in their trafficking to and entry into the nucleus (Fig. 6B).

Native Western dot blot experiments were used to investigate the possibility that ADK8 impairs AAV8 trafficking by blocking exposure of VP1u, which is predicted to be localized inside the capsid prior to exposure to the low pH of the endosome. VP1u contains a phospholipase A2 (PLA2) domain required for endocytic pathway release and nuclear localization signals (25, 28, 66, 68). The A1 MAb, which recognizes the AAV2 VP1u residues 123 to 131 (VP1 numbering), is cross-reactive against several AAV serotypes (81), including AAV8 and was used to monitor VP1 externalization in the presence or absence of ADK8. Incubation of rAAV2, rAAV8, and $rAAV2_{585RGNRQ589\rightarrow QQNTA}$ particles with or without ADK8 at 37°C for 5 min showed no reactivity with A1 (Fig. 8). However, the A1 epitope was detected in rAAV2 and $rAAV2_{585RGNRQ589\rightarrow QQNTA}$ after incubation at 65°C for 5 min, and weakly detected in rAAV8 in the absence of antibody (Fig. 8, left panel). Heat treatment of rAAV8 particles preincubated with ADK8 at 65°C appeared to increase VP1u detection by A1 (Fig. 8, right panel). After treatment at 71°C, the A1 signal was detected for all three viruses. These data indicate that, in this *in vitro* assay, the ADK8 antibody does not prevent externalization of VP1u. Hence, ADK8 neutralization of AAV8 *in vivo* may not involve a mechanism in which endosome release is prevented.

Previous AAV trafficking and mutagenesis studies have shown that an ordered set of events following cell entry, including exposure to the low pH of the endocytic pathway, lead to exposure of VP1u so it can perform its PLA2 and NLS functions, which are prerequisites for nuclear entry and successful infection (27, 66). The cell binding and trafficking results indicate that ADK8 does not influence AAV8 binding to receptor but does have a small effect on internalization and a major impact on perinuclear accumulation and possibly nuclear entry. This most likely is not the result of inhibition of PLA2 activity, because ADK8 does not pre-

vent VP1u externalization, at least not *in vitro*. Thus far, no structural element of the AAV capsid has been identified as having an effect on intracellular trafficking (including perinuclear accumulation) of the virus. This accumulation may be a passive event, in the sense that, if virus particles enter the correct endosomal compartment, they are automatically transported into the perinuclear area. However, growing evidence suggests that endocytosed cargo has an influence on the destination of the vesicles (10, 61). Our results indicate that the AAV protrusions may play a role in directing intracellular vesicle transport to the right destination, either by selecting the right entry pathway or possibly by interacting with transmembrane receptors during vesicle transport. If the ADK8 antibody blocks such interactions, vesicle transport may cease or be misdirected. Recent reports also suggest that the AAVs can enter cells by multiple pathways and that if internalization is redirected into less efficient pathways transduction is inhibited (56). It is possible that this is what happens to AAV8 following ADK8 binding. Also, ADK8 binding to the AAV8 protrusions could indirectly affect the conformation of the 5-fold channel or the 2-fold dimple, and this in turn could influence postentry trafficking. The detailed mechanism by which ADK8 neutralizes AAV8 certainly requires further investigation. However, we have clearly demonstrated here that the binding of an antibody to the capsid protrusion(s) strongly influences intracellular trafficking and prevents the perinuclear accumulation of AAV8.

Impact on rAAV8 vector generation. The preexistence of immune responses in humans has proven to be a challenge in efforts to produce effective gene delivery vectors. Previous reports indicate that the seroprevalence of AAV8 is lower than AAV1 and AAV2 in the human population (11, 13) and, although preexisting antibodies could impede gene transfer by AAV8 (34), the extent of the T-cell-based response is lower than those noted for related serotypes (47). Thus, AAV8 has considerable potential as a clinical, therapeutic gene delivery vector (6, 37, 54).

Current strategies to circumvent immune responses to AAVs include shuffling of the *cap* gene to produce chimeric vectors, generating wild-type capsids under immunoselective selection, and identifying natural AAVs from other animal species (24, 41, 49, 64). This is in fact how AAV8 was identified (23, 24). However, preliminary characterization of many other identified AAV sequences show poor capsid production, as well as reduced packaging and altered infectivity profiles, which significantly limits the number of viable vectors (71). Studies aimed at locating and characterizing functional regions on the capsid surfaces of viable serotypes have identified VRs that are necessary for structural integrity, receptor binding, infectivity, and antigenicity. All of these studies have enhanced our understanding of AAV basic biology. However, genetic engineering of the capsid as a means to improve AAV as a vector is only fruitful if it succeeds in generating vectors that mimic or exceed wt virus production and transduction properties and can also evade surveillance of the host immune system. Structural information about antigenic regions of the capsid, such as that reported here, can guide this effort. AAV2 MAbs such as A20 and C37-B have been produced and characterized (80), and the repertoire of anti-AAV MAbs has increased recently (32, 40, 67). Despite this, little is known about the antigenic structure of AAVs. The present study of AAV8-ADK8 is the first report to our knowledge of the structure of an AAV-Fab complex, and it has identified a VR on the AAV8 capsid surface that is specifically important for its antigenicity. Notably, this antigenic site does not affect receptor binding and thus provides a 3D platform for vector development using mutational analysis aimed at generating antigenic escape vectors that retain their natural tissue transduction efficiency. This is an important requirement for improving the efficacy of gene delivery by viral vectors, especially in circumstances where multiple injections of a therapeutic vector may be required.

ACKNOWLEDGMENTS

This project was funded in part by NIH grants R21AI072341 (to M.A.-M.), R01 GM082946 (to M.A.-M.), R37 GM033050 (to T.S.B.), and 1S10 RR020016 (to T.S.B.), and by support from the University of California, San Diego (UCSD), and the Agouron Foundation (to T.S.B.) to establish cryo-EM facilities at UCSD. J.A.K. was supported by grant KL516/7-1 from the Deutsche Forschungsgemeinschaft. Molecular graphics and analyses were performed with the UCSF Chimera package. Chimera is developed by the Resource for Biocomputing, Visualization, and Informatics at the University of California, San Francisco, with support from the National Institutes of Health (National Center for Research Resources grant 2P41RR001081 and National Institute of General Medical Sciences grant 9P41GM103311).

REFERENCES

1. **Agbandje-McKenna M, Chapman MS.** 2006. Correlating structure with function in the viral capsid, p 125–139. *In* Kerr JR, et al. (ed), Parvoviruses. Edward Arnold, Ltd, New York, NY.
2. **Agbandje-McKenna M, Kleinschmidt J.** 2011. AAV capsid structure and cell interactions. Methods Mol. Biol. **807**:47–92.
3. **Akache B, et al.** 2006. The 37/67-kilodalton laminin receptor is a receptor for adeno-associated virus serotypes 8, 2, 3, and 9. J. Virol. **80**:9831–9836.
4. **Asokan A, et al.** 2010. Reengineering a receptor footprint of adeno-associated virus enables selective and systemic gene transfer to muscle. Nat. Biotechnol. **28**:79–82.
5. **Baker TS, Olson NH, Fuller SD.** 1999. Adding the third dimension to virus life cycles: three-dimensional reconstruction of icosahedral viruses from cryo-electron micrographs. Microbiol. Mol. Biol. Rev. **63**:862–922.
6. **Balazs AB, et al.** 2011. Antibody-based protection against HIV infection by vectored immunoprophylaxis. Nature **481**:81–84.
7. **Bell P, et al.** 2011. Evaluation of adeno-associated viral vectors for liver-directed gene transfer in dogs. Hum. Gene Ther. **22**:985–997.
8. **Blacklow NR, et al.** 1971. A seroepidemiologic study of adenovirus-associated virus infection in infants and children. Am. J. Epidemiol. **94**:359–366.
9. **Bleker S, Sonntag F, Kleinschmidt JA.** 2005. Mutational analysis of narrow pores at the fivefold symmetry axes of adeno-associated virus type 2 capsids reveals a dual role in genome packaging and activation of phospholipase A2 activity. J. Virol. **79**:2528–2540.
10. **Bonifacino JS, Traub LM.** 2003. Signals for sorting of transmembrane proteins to endosomes and lysosomes. Annu. Rev. Biochem. **72**:395–447.
11. **Boutin S, et al.** 2010. Prevalence of serum IgG and neutralizing factors against adeno-associated virus (AAV) types 1, 2, 5, 6, 8, and 9 in the healthy population: implications for gene therapy using AAV vectors. Hum. Gene Ther. **21**:704–712.
12. **Bowman VD, et al.** 2002. An antibody to the putative aphid recognition site on cucumber mosaic virus recognizes pentons but not hexons. J. Virol. **76**:12250–12258.
13. **Calcedo R, Vandenberghe LH, Gao G, Lin J, Wilson JM.** 2009. Worldwide epidemiology of neutralizing antibodies to adeno-associated viruses. J. Infect. Dis. **199**:381–390.
14. **Chacon P, Wriggers W.** 2002. Multi-resolution contour-based fitting of macromolecular structures. J. Mol. Biol. **317**:375–384.
15. **Chapman MS, Agbandje-McKenna M.** 2006. Atomic structures of viral particles, p 107–123. *In* Kerr JR, et al. (ed), Parvoviruses. Edward Arnold, Ltd, New York, NY.
16. **Chen J, Wu Q, Yang P, Hsu H-C, Mountz JD.** 2006. Determination of specific CD4 and CD8 T cell epitopes after AAV2- and AAV8-hF.IX gene therapy. Mol. Ther. **13**:260–269.
17. **Chirmule N, et al.** 1999. Immune responses to adenovirus and adeno-associated virus in humans. Gene Ther. **6**:1574–1583.

18. **Davidoff AM, et al.** 2005. Comparison of the ability of adeno-associated viral vectors pseudotyped with serotype 2, 5, and 8 capsid proteins to mediate efficient transduction of the liver in murine and nonhuman primate models. Mol. Ther. **11**:875–888.
19. **Davies DR, Cohen GH.** 1996. Interactions of protein antigens with antibodies. Proc. Natl. Acad. Sci. U. S. A. **93**:7–12.
20. **De BP, et al.** 2006. High levels of persistent expression of alpha1-antitrypsin mediated by the nonhuman primate serotype rh.10 adeno-associated virus despite preexisting immunity to common human adeno-associated viruses. Mol. Ther. **13**:67–76.
21. **Dubielzig R, King JA, Weger S, Kern A, Kleinschmidt JA.** 1999. Adeno-associated virus type 2 protein interactions: formation of pre-encapsidation complexes. J. Virol. **73**:8989–8998.
22. **Erles K, Sebokova P, Schlehofer JR.** 1999. Update on the prevalence of serum antibodies (IgG and IgM) to adeno-associated virus (AAV). J. Med. Virol. **59**:406–411.
23. **Gao G-P, et al.** 2002. Novel adeno-associated viruses from rhesus monkeys as vectors for human gene therapy. Proc. Natl. Acad. Sci. U. S. A. **99**:11854–11859.
24. **Gao G, Vandenberghe LH, Wilson JM.** 2005. New recombinant serotypes of AAV vectors. Curr. Gene Ther. **5**:285–297.
25. **Girod A, et al.** 2002. The VP1 capsid protein of adeno-associated virus type 2 is carrying a phospholipase A2 domain required for virus infectivity. J. Gen. Virol. **83**:973–978.
26. **Govindasamy L, et al.** 2006. Structurally mapping the diverse phenotype of adeno-associated virus serotype 4. J. Virol. **80**:11556–11570.
27. **Grieger JC, Johnson JS, Gurda-Whitaker B, Agbandje-McKenna M, Samulski RJ.** 2007. Surface-exposed adeno-associated virus Vp1-NLS capsid fusion protein rescues infectivity of noninfectious wild-type Vp2/Vp3 and Vp3-only capsids but not that of fivefold pore mutant virions. J. Virol. **81**:7833–7843.
28. **Grieger JC, Snowdy S, Samulski RJ.** 2006. Separate basic region motifs within the adeno-associated virus capsid proteins are essential for infectivity and assembly. J. Virol. **80**:5199–5210.
29. **Grimm D, Kay MA.** 2003. From virus evolution to vector revolution: use of naturally occurring serotypes of adeno-associated virus (AAV) as novel vectors for human gene therapy. Curr. Gene Ther. **3**:281–304.
30. **Grimm D, et al.** 1999. Titration of AAV-2 particles via a novel capsid ELISA: packaging of genomes can limit production of recombinant AAV-2. Gene Ther. **6**:1322–1330.
31. **Grimm D, et al.** 2008. In vitro and in vivo gene therapy vector evolution via multispecies interbreeding and retargeting of adeno-associated viruses. J. Virol. **82**:5887–5911.
32. **Harbison CE, et al.** 2011. Examining the cross-reactivity and neutralization mechanisms of a panel of monoclonal antibodies against adeno-associated virus serotypes 1 and 5. J. Gen. Virol. **93**:347–355.
33. **Harlow E, Lane D.** 1988. Antibodies laboratory manual, p 321–358. Cold Spring Harbor Laboratory, Cold Spring Harbor, NY.
34. **Hurlbut GD, et al.** 2010. Preexisting immunity and low expression in primates highlight translational challenges for liver-directed AAV8-mediated gene therapy. Mol. Ther. **18**:1983–1994.
35. **Kleywegt GJ, Jones TA.** 1996. xdlMAPMAN and xdlDATAMAN: programs for reformatting, analysis and manipulation of biomacromolecular electron-density maps and reflection data sets. Acta Crystallogr. D Biol. Crystallogr. **52**:826–828.
36. **Knowles BB, Howe CC, Aden DP.** 1980. Human hepatocellular carcinoma cell lines secrete the major plasma proteins and hepatitis B surface antigen. Science **209**:497–499.
37. **Koo T, et al.** 2011. Long-term functional adeno-associated virus-microdystrophin expression in the dystrophic CXMDj dog. J. Gene Med. **13**:497–506.
38. **Krissinel E, Henrick K.** 2007. Inference of macromolecular assemblies from crystalline state. J. Mol. Biol. **372**:774–797.
39. **Kronenberg S, Böttcher B, von der Lieth CW, Bleker S, Kleinschmidt JA.** 2005. A conformational change in the adeno-associated virus type 2 capsid leads to the exposure of hidden VP1 N termini. J. Virol. **79**:5296–5303.
40. **Kuck D, Kern A, Kleinschmidt JA.** 2007. Development of AAV serotype-specific ELISAs using novel monoclonal antibodies. J. Virol. Methods **140**:17–24.
41. **Kwon I, Schaffer DV.** 2008. Designer gene delivery vectors: molecular engineering and evolution of adeno-associated viral vectors for enhanced gene transfer. Pharm. Res. **25**:489–499.
42. **Lane MD, et al.** 2005. Production, purification, crystallization, and preliminary X-ray analysis of adeno-associated virus serotype 8. Acta Crystallogr. Sect. F. Struct. Biol. Crystallogr. Commun. **61**:558–561.
43. **Lerch TF, Xie Q, Chapman MS.** 2010. The structure of adeno-associated virus serotype 3B (AAV-3B): insights into receptor binding and immune evasion. Virology **403**:26–36.
44. **Lochrie MA, et al.** 2006. Mutations on the external surfaces of adeno-associated virus type 2 capsids that affect transduction and neutralization. J. Virol. **80**:821–834.
45. **Manno CS, et al.** 2006. Successful transduction of liver in hemophilia by AAV-Factor IX and limitations imposed by the host immune response. Nat. Med. **12**:342–347.
46. **Margaritis P, et al.** 2009. Successful treatment of canine hemophilia by continuous expression of canine FVIIa. Blood **113**:3682–3689.
47. **Mays LE, et al.** 2009. Adeno-associated virus capsid structure drives CD4-dependent $CD8^+$ T cell response to vector encoded proteins. J. Immunol. **182**:6051–6060.
48. **Mingozzi F, High KA.** 2011. Therapeutic in vivo gene transfer for genetic disease using AAV: progress and challenges. Nat. Rev. Genet. **12**:341–355.
49. **Mitchell AM, Nicolson SC, Warischalk JK, Samulski RJ.** 2010. AAV's anatomy: roadmap for optimizing vectors for translational success. Curr. Gene Ther. **10**:319–340.
50. **Moskalenko M, et al.** 2000. Epitope mapping of human anti-adeno-associated virus type 2 neutralizing antibodies: implications for gene therapy and virus structure. J. Virol. **74**:1761–1766.
51. **Muller OJ, et al.** 2003. Random peptide libraries displayed on adeno-associated virus to select for targeted gene therapy vectors. Nat. Biotechnol. **21**:1040–1046.
52. **Nakai H, et al.** 2005. Unrestricted hepatocyte transduction with adeno-associated virus serotype 8 vectors in mice. J. Virol. **79**:214–224.
53. **Nam H-J, et al.** 2007. Structure of adeno-associated virus serotype 8, a gene therapy vector. J. Virol. **81**:12260–12271.
54. **Nathwani AC, et al.** 2011. Adenovirus-associated virus vector-mediated gene transfer in hemophilia B. N. Engl. J. Med. **365**:2357–2365.
55. **Ng R, et al.** 2010. Structural characterization of the dual glycan binding adeno-associated virus serotype 6. J. Virol. **84**:12945–12957.
56. **Nonnenmacher M, Weber T.** 2012. Intracellular transport of recombinant adeno-associated virus vectors. Gene Ther. **19**:649–658.
57. **Padron E, et al.** 2005. Structure of adeno-associated virus type 4. J. Virol. **79**:5047–5058.
58. **Pear WS, Nolan GP, Scott ML, Baltimore D.** 1993. Production of high-titer helper-free retroviruses by transient transfection. Proc. Natl. Acad. Sci. U. S. A. **90**:8392–8396.
59. **Pettersen EF, et al.** 2004. UCSF Chimera–a visualization system for exploratory research and analysis. J. Comput. Chem. **25**:1605–1612.
60. **Pintilie GD, Zhang J, Goddard TD, Chiu W, Gossard DC.** 2010. Quantitative analysis of cryo-EM density map segmentation by watershed and scale-space filtering, and fitting of structures by alignment to regions. J. Struct. Biol. **170**:427–438.
61. **Puthenveedu MA, von Zastrow M.** 2006. Cargo regulates clathrin-coated pit dynamics. Cell **127**:113–124.
62. **Sarkar R, et al.** 2004. Total correction of hemophilia A mice with canine FVIII using an AAV 8 serotype. Blood **103**:1253–1260.
63. **Scallan CD, et al.** 2006. Human immunoglobulin inhibits liver transduction by AAV vectors at low AAV2 neutralizing titers in SCID mice. Blood **107**:1810–1817.
64. **Schaffer DV, Koerber JT, Lim KI.** 2008. Molecular engineering of viral gene delivery vehicles. Annu. Rev. Biomed. Eng. **10**:169–194.
65. **Shen X, Storm T, Kay MA.** 2007. Characterization of the relationship of AAV capsid domain swapping to liver transduction efficiency. Mol. Ther. J. Am. Soc. Gene Ther. **15**:1955–1962.
66. **Sonntag F, Bleker S, Leuchs B, Fischer R, Kleinschmidt JA.** 2006. Adeno-associated virus type 2 capsids with externalized VP1/VP2 trafficking domains are generated prior to passage through the cytoplasm and are maintained until uncoating occurs in the nucleus. J. Virol. **80**:11040–11054.
67. **Sonntag F, et al.** 2011. The assembly-activating protein promotes capsid assembly of different adeno-associated virus serotypes. J. Virol. **85**:12686–12697.
68. **Stahnke S, et al.** 2011. Intrinsic phospholipase A2 activity of adeno-associated virus is involved in endosomal escape of incoming particles. Virology **409**:77–83.

69. **Suh SW, et al.** 1986. The galactan-binding immunoglobulin Fab J539: an X-ray diffraction study at 2.6-Å resolution. Proteins **1**:74–80.
70. **Thomas CE, Storm TA, Huang Z, Kay MA.** 2004. Rapid uncoating of vector genomes is the key to efficient liver transduction with pseudotyped adeno-associated virus vectors. J. Virol. **78**:3110–3122.
71. **Vandenberghe LH, et al.** 2009. Naturally occurring singleton residues in AAV capsid impact vector performance and illustrate structural constraints. Gene Ther. **16**:1416–1428.
72. **Veldwijk MR, et al.** 2002. Development and optimization of a real-time quantitative PCR-based method for the titration of AAV-2 vector stocks. Mol. Ther. **6**:272–278.
73. **Wang L, et al.** 2011. AAV8-mediated hepatic gene transfer in infant rhesus monkeys (*Macaca mulatta*). Mol. Ther. **19**:2012–2020.
74. **Wang L, et al.** 2011. Liver gene transfer with vectors based on adeno-associated virus 8 in non-human primates: impact of pre-existing immunity. Hum. Gene Ther. **22**:1389–1401.
75. **Wang L, et al.** 2010. The pleiotropic effects of natural AAV infections on liver-directed gene transfer in macaques. Mol. Ther. **18**:126–134.
76. **Wang L, et al.** 2010. Systematic evaluation of AAV vectors for liver directed gene transfer in murine models. Mol. Ther. **18**:118–125.
77. **Weger S, Wistuba A, Grimm D, Kleinschmidt JA.** 1997. Control of adeno-associated virus type 2 cap gene expression: relative influence of helper virus, terminal repeats, and Rep. proteins. J. Virol. **71**:8437–8447.
78. **Wikoff WR, et al.** 1994. The structure of a neutralized virus: canine parvovirus complexed with neutralizing antibody fragment. Structure **2**:595–607.
79. **Wilson IA, Stanfield RL.** 1994. Antibody-antigen interactions: new structures and new conformational changes. Curr. Opin. Struct. Biol. **4**:857–867.
80. **Wistuba A, Kern A, Weger S, Grimm D, Kleinschmidt JA.** 1997. Subcellular compartmentalization of adeno-associated virus type 2 assembly. J. Virol. **71**:1341–1352.
81. **Wobus CE, et al.** 2000. Monoclonal antibodies against the adeno-associated virus type 2 (AAV-2) capsid: epitope mapping and identification of capsid domains involved in AAV-2-cell interaction and neutralization of AAV-2 infection. J. Virol. **74**:9281–9293.
82. **Xie Q, et al.** 2002. The atomic structure of adeno-associated virus (AAV-2), a vector for human gene therapy. Proc. Natl. Acad. Sci. U. S. A. **99**: 10405–10410.
83. **Yan X, Dryden KA, Tang J, Baker TS.** 2007. *Ab initio* random model method facilitates 3D reconstruction of icosahedral particles. J. Struct. Biol. **157**:211–225.
84. **Yan X, Sinkovits RS, Baker TS.** 2007. AUTO3DEM–an automated and high throughput program for image reconstruction of icosahedral particles. J. Struct. Biol. **157**:73–82.
85. **Ying Y, et al.** 2010. Heart-targeted adeno-associated viral vectors selected by in vivo biopanning of a random viral display peptide library. Gene Ther. **17**:980–990.
86. **Yu CY, et al.** 2009. A muscle-targeting peptide displayed on AAV2 improves muscle tropism on systemic delivery. Gene Ther. **16**:953–962.
87. **Zhang X, Walker SB, Chipman PR, Nibert ML, Baker TS.** 2003. Reovirus polymerase lambda 3 localized by cryo-electron microscopy of virions at a resolution of 7.6 Å. Nat. Struct. Biol. **10**:1011–1018.
88. **Zincarelli C, Soltys S, Rengo G, Rabinowitz JE.** 2008. Analysis of AAV serotypes 1–9 mediated gene expression and tropism in mice after systemic injection. Mol. Ther. **16**:1073–1080.
89. **Zolotukhin S, et al.** 1999. Recombinant adeno-associated virus purification using novel methods improves infectious titer and yield. Gene Ther. **6**:973–985.
90. **Zolotukhin S, Potter M, Hauswirth WW, Guy J, Muzyczka N.** 1996. A "humanized" green fluorescent protein cDNA adapted for high-level expression in mammalian cells. J. Virol. **70**:4646–4654.